Earth and Planetary Science Letters 319-320 (2012) 96–103

Contents lists available at SciVerse ScienceDirect

Earth and Planetary Science Letters

journal homepage: www.elsevier.com/locate/epsl

On the increase in thermal diffusivity caused by the perovskite to post-perovskite phase transition and its implications for mantle dynamics

Simon A. Hunt [a,b,c,*], D. Rhodri Davies [d], Andrew M. Walker [e], Richard J. McCormack [a], Andrew S. Wills [c], David P. Dobson [a], Li Li [b]

[a] Department of Earth Sciences, University College London, Gower Street, London, WC1E 6BT, UK
[b] Mineral Physics Institute, Dept. Geosci., SUNY Stony Brook, Stony Brook, NY 11790, USA
[c] Department of Chemistry, University College London, 20 Gordon Street, London, WC1H 0AJ, UK
[d] Department of Earth Science and Engineering, Imperial College London, SW7 2AZ, UK
[e] Department of Earth Sciences, University of Bristol, Wills Memorial Building, Queen's Road, Bristol, BS8 1RJ, UK

ARTICLE INFO

Article history:
Received 30 September 2011
Received in revised form 1 December 2011
Accepted 4 December 2011
Available online 21 January 2012

Editor: T. Spohn

Keywords:
D double-prime (D″)
Thermal diffusivity
Ångström method
$CaIrO_3$
Post-perovskite
Perovskite

ABSTRACT

The thermal diffusivity (κ) of perovskite and post-perovskite $CaIrO_3$ has been measured, at elevated pressure and temperatures up to 600 °C, using the X-radiographic Ångström method. At high temperatures we find that the thermal diffusivity of post-perovskite is slightly below twice that of isochemical perovskite over the temperature range investigated. Assuming a similar effect occurs in $MgSiO_3$ post-perovskite, the effect of the contrasting thermal transport properties between perovskite and post-perovskite on mantle dynamics has been investigated using simple two-dimensional convection models. These show a reduction in extent and increase in depth of post-perovskite lenses, as well as increased core–mantle-boundary heat-flux, broader upwellings and more vigorous downwellings when compared to the reference, constant *a*, case.

© 2011 Elsevier B.V. Open access under CC BY license.

1. Introduction

The D″ region, at the base of Earth's mantle, is known to be both anomalous and crucial to our understanding of mantle dynamics and Earth's evolution. This ~200 km thick layer contains superadiabatic thermal gradients in excess of 1000 K, is the region in which some mantle upwellings are thought to originate (Schubert et al., 2001), and may act as a graveyard for subducted slabs. Key to unravelling the dynamical behaviour of this region, and indeed the whole mantle, is the quest to elucidate the physical properties of its constituent materials. Since the discovery of a post-perovskite phase in $MgSiO_3$, stable at pressures in excess of ~110 GPa (Murakami et al., 2004; Oganov and Ono, 2004), the presence of this $CaIrO_3$-structured material has been able to explain many of the lowermost-mantle's properties. For example, the seismic anisotropy of D″ (e.g. Garnero and Lay, 2003; Panning and Romanowicz, 2004) can be explained by a lattice preferred orientation in post-perovskite (e.g. Walker et al., 2011) and the low viscosity of this layer implied by geoid modelling (Tosi et al., 2009) is consistent with the results of both experimental (Hunt et al., 2009, with $CaIrO_3$) and computational studies (Ammann et al., 2010, for $MgSiO_3$), which show that post-perovskite is rheologically weaker than isochemical perovskite. In order to model and understand the dynamics of D″ and its effect on the rest of the planet, it is necessary to determine the rheology, density, thermal expansion and thermal diffusivity of both perovskite and post-perovskite. Whilst the unit cell volumes, hence density, and thermal expansion of both $MgSiO_3$–perovskite and post-perovskite have been measured (e.g. Guignot et al., 2007; Komabayashi et al., 2008), the absolute or even relative thermal transport properties of $MgSiO_3$–perovskite and post-perovskite are, at best, poorly constrained.

To date, the thermal diffusivity of $MgSiO_3$–perovskite has been measured by: (i) Osako and Ito (1991), at ambient pressure and at temperatures below room temperature; and (ii) Manthilake et al. (2011), who measured the thermal diffusivity at 26 GPa and up to 800 °C. As well as these measurements, Hofmeister (2010) measured the themal diffusivity of a wide range of perovskite structured phases but the thermal diffusivity of post-perovskites is much less extensively measured. Only two studies report the thermal transport properties of both a perovskite and post-perovskite. In the first of these, Keawprak et al. (2009) measured the thermal conductivity of 60% dense compacts of both perovskite and post-perovskite structured $CaIrO_3$. They found that, at room temperature, the conductivity of post-perovskite is around twice that of perovskite. With increasing

* Corresponding author at: Department of Earth Sciences, University College London, Gower Street, London, WC1E 6BT, UK.
E-mail address: simon.hunt@ucl.ac.uk (S.A. Hunt).

0012-821X © 2011 Elsevier B.V. Open access under CC BY license.
doi:10.1016/j.epsl.2011.12.009

temperature their measured values converge and above 350 °C both phases have virtually indistinguishable thermal transport properties. The other study by Cheng et al. (2011) used the (Ca,Sr)IrO_3 system, at and below ambient temperature, showing that $CaIrO_3$–post-perovskite has approximately three times the thermal conductivity of $SrIrO_3$–perovskite. These measurements, whilst not perfect, support the prediction of Hofmeister (2007) that the thermal diffusivity of $MgSiO_3$–post-perovskite is a factor of ≈1.6 larger than that of $MgSiO_3$–perovskite.

Even a relatively small difference between the thermal transport properties of perovskite and post-perovskite could have a significant effect on the heat flow across the core-mantle boundary, potentially influencing whole mantle convection and Earth's thermal evolution. $CaIrO_3$ has been used extensively in previous studies as a structural (e.g. Lindsay-Scott et al., 2007; Martin et al., 2007) and mechanical (e.g. Hunt et al., 2009; Walte et al., 2007; Yamazaki et al., 2006) analogue for $MgSiO_3$–perovskite and post-perovskite. Here, however, we use it to investigate the relative thermal transport properties of perovskite and post-perovskite structure types using the recently developed X-radiographic Ångström method (Dobson et al., 2008, 2010; Hunt et al., 2011). We then use simple two-dimensional convection models to explore the first-order effect on the mantle of post-perovskite with a distinct thermal diffusivity.

2. Experimental method

In the Ångström method a thermal standing wave is set up in a sample by sinusoidally perturbing the temperature generated by a furnace. In previous high-pressure implementations of the Ångström method (e.g. Katsura, 1993, 1995; Xu et al., 2004) a cylindrical furnace was used to co-axially surround the sample and generate in it a thermal standing wave. Two thermocouples were placed in the sample to measure this thermal wave, one on the axis ($R \approx 0$) and the other at a finite radius ($R \neq 0$). The sinusoidal temperature profile recorded by the central thermocouple has phase (Φ_0) and amplitude (θ_0) which is related to the phase (Φ_R) and amplitude (θ_R) measured in the radial thermocouple by the thermal diffusivity (κ) and the frequency of the temperature perturbation (f). If the sample is sufficiently long that an infinite cylinder approximation is valid (i.e. the heat flow is perpendicular to the axis of the furnace) the difference between the phases (Φ) and the ratio of the amplitudes (θ) is related to the thermal diffusivity as follows (Khedari et al., 1995):

$$\Phi = \Phi_0 - \Phi_R = \tan^{-1}\left(\frac{\mathrm{bei}A}{\mathrm{ber}A}\right) \tag{1a}$$

$$\theta = \frac{\theta_0}{\theta_R} = \frac{1}{\sqrt{\mathrm{ber}^2 A + \mathrm{bei}^2 A}} \tag{1b}$$

where

$$A = R\left(\frac{2\pi f}{\kappa}\right)^{1/2} = R\left(\frac{\omega}{\kappa}\right)^{1/2}, \tag{1c}$$

bei and ber are the zeroth order Kelvin functions and ω is the angular frequency of the temperature perturbation. In practice, it has been found that the ratio of the amplitudes (θ, Eq. (1b)) gives less accurate results than those calculated from the difference between the phases (Φ, Eq. (1a), e.g. Katsura, 1993, 1995).

In the X-radiographic Ångström method used here, the thermocouples are replaced with 100 μm wide strips of 12 μm thick Pt foil which are placed across the diameter of the sample and perpendicular to the synchrotron X-ray beam. The Pt strips are displaced by thermal expansion and contraction of the sample in response to the applied sinusoidally varying thermal field and these displacements are monitored X-radiographically. The variation in sample length is used as a proxy for mean temperature in the sample at each radius and can be used to find the thermal diffusivity in the same way as with the two thermocouples. For a more detailed discussion of this methodology and its merits see Hunt et al. (2011).

2.1. Experimental procedure

Two X-radiography experiments were performed for this study, using beam-line X17B2, at the National Synchrotron Light Source in Brookhaven National Laboratory: the first with a perovskite structured $CaIrO_3$ sample (CaI_18) and the second with a post-perovskite structured $CaIrO_3$ sample (CaI_19).

The samples for both experiments were presynthesised from a mixture of CaO and IrO_2. The perovskite sample was synthesised, in a piston-cylinder device, at 1 GPa and 1425 °C for 2 h whilst the post-perovskite sample was synthesised, using a Kawai-type multi-anvil device, at 3 GPa and 1350 °C for 20 h. Laboratory X-ray diffraction measurements of both samples showed complete reaction to the intended product with a small amount (≈2%) of residual IrO_2. The excess IrO_2 is intentionally present in the samples as it promotes formation of $CaIrO_3$ over higher, more Ca rich, oxides (e.g. $Ca2IrO_4$, Lindsay-Scott et al., 2007).

The thermal diffusivity measurements were performed using T-cup tooling (Vaughan et al., 1998) in the 250-tonne SAM85 press, in conjuction with a Prosilica visible light camera and fluorescent YAG crystal. The 8 mm edge-length octahedral experimental cell (Fig. 1a) used a combined platinum–graphite furnace which consisted of a 12 μm thick platinum foil cylinder inside the standard straight graphite furnace. This furnace design was necessary to prevent the $CaIrO_3$ samples being reduced by the graphite. Samples of $CaIrO_3$ are opaque to X-rays and therefore thin (≈300 μm thick) MgO discs were placed between the sample and the Pt strips in order that the strips could be properly imaged. Discs of NaCl were placed next to the MgO because NaCl is more compressible than both the sample and MgO and is therefore compressed by the thermal expansion of the sample, allowing the thermal standing wave to the measured. A D-type Tungsten–Rhenium thermocouple was placed radially in the cell with the hot junction butted up to, but insulated from, the outside of the furnace. For each experiment 4 X-ray transparent cubic Boron Nitride (CBN) anvils and 4 edge-length Tungsten Carbide anvils were used, each with a 4 mm truncation and 10 mm edge length. The geometry of the T-Cup allows the entire sample to be imaged with the use of only 4 transparent anvils which minimises the use of expensive CBN anvils (Fig. **1**b).

Each X-radiography experiment was cold compressed to an end-load of 53.4 kN (approximately 0.5 GPa) and then heated step-wise, in 50 °C increments. At each temperature, thermal perturbations of 30–50 °C were generated with nominal periods of 8, 4, 2, 1 and 0.5 s by sinusoidally varying the current applied to the furnace. The temperature oscillations were started between 5 and 10 periods before data collection commenced thereby ensuring the thermal standing wave was properly formed. For each period, 1000 X-radiography images were collected at approximately ten frames per period; a typical image is shown in Fig. 2, along with a line drawing illustrating what is observed in the image. Due to the camera trigger not being synchronised with the temperature oscillations the phase angle at which the images were collected aliased through all phase angles in the course of each data collection. X-ray diffraction patterns were acquired periodically throughout the experiments, between data collections, to ascertain whether the sample had decomposed or transformed. The samples were recovered and prepared for S.E.M. analysis to determine the sample characteristics at the end of the experiment.

2.2. Data analysis

The displacements of the foils were calculated at 20 radii across each foil (boxes in Fig. **2**a) using the same cross-correlation routine

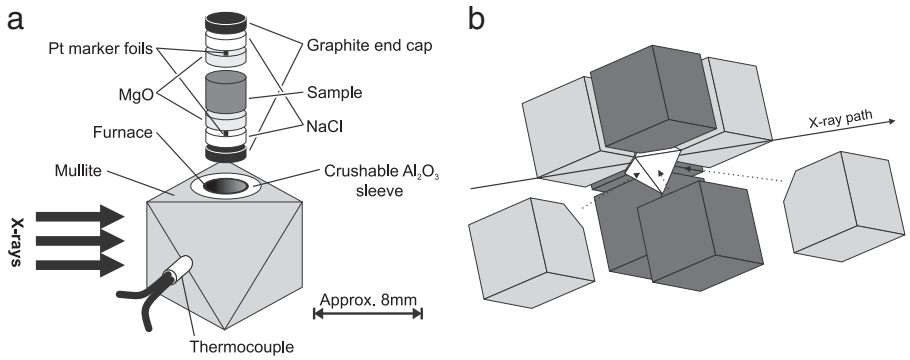

Fig. 1. (a) Illustration of the cell design used in these experiments. (b) T-cup anvil arrangement showing that only 4 CBN anvils are necessary in each experiment. White: experimental cell (this is the octahedral cell illustrated in (a)); Dark grey: tungsten carbide anvils; pale grey: Cubic Boron Nitride anvils.

used by Hunt et al. (2011). The vertical displacement of the foil within each box was calculated by finding the minimum in the Sum of Squared Differences (SSD) for each box relative to that of the same box in a reference image, which was taken as the middle image of each data collection. Each displacement, therefore, is an independent measurement, so an erroneous displacement calculation between two boxes does not propagate into other displacements and can be discarded later.

The platinum foil of the furnace and the X-ray transparent anvils both contribute to the background of the X-radiography images, reducing the contrast between the background and the foil. The shadow of the Pt foil above the sample in experiment CaI_19 (boxes 1–20 in Fig. 2) was obscured by the furnace to such a degree that the displacement data was dominated by noise. This makes the length changes in the sample, which are calculated from the displacements of the top and bottom foils, unreliable. However, the displacements of a single foil can be used to solve for the thermal diffusivity. The displacement of the single foil can be thought of as changes in sample length from a non-deforming plane in the centre of the sample and doing this will not affect the phase lags. To verify that the single foils give comparable thermal diffusivities to the length changes, the thermal diffusivity of the sample in experiment CaI_18 was calculated from both the single foil displacements and the length changes: thermal diffusivities estimated by the two methods agree within two standard errors. In order to permit direct comparison of the data sets the single foil data from CaI_18 is regarded as the definitive version of the data.

The single foil displacements and sample length changes exhibit secular variation in position during the course of each data collection. In previous studies using this method, a moving average over two periods ($2/f$) was subtracted from the length changes to remove any secular variation in the sample length. Here, however, a smoothing quadratic spline was used to remove the secular variation in displacement (Fig. 3a). The advantage of the smoothing spline is that the calculated background does not have a frequency component which is the same as that of the thermal oscillations.

The resulting detrended displacements (d), at each radius (R), are fitted to:

$$d_{R,t} = \theta_R \sin(\omega t + \Phi_R) \tag{2}$$

where t is the time of acquisition for each image. Eq. (2) is fitted to the displacements at all radii simultaneously by minimising the SSD with a single period but independent amplitudes and phases for each radius. Erroneous displacements have a disproportionally large effect on the SSD value, therefore during the fitting displacement values with a residual (|datum − fit|) of more than 4 standard deviations are treated as outliers

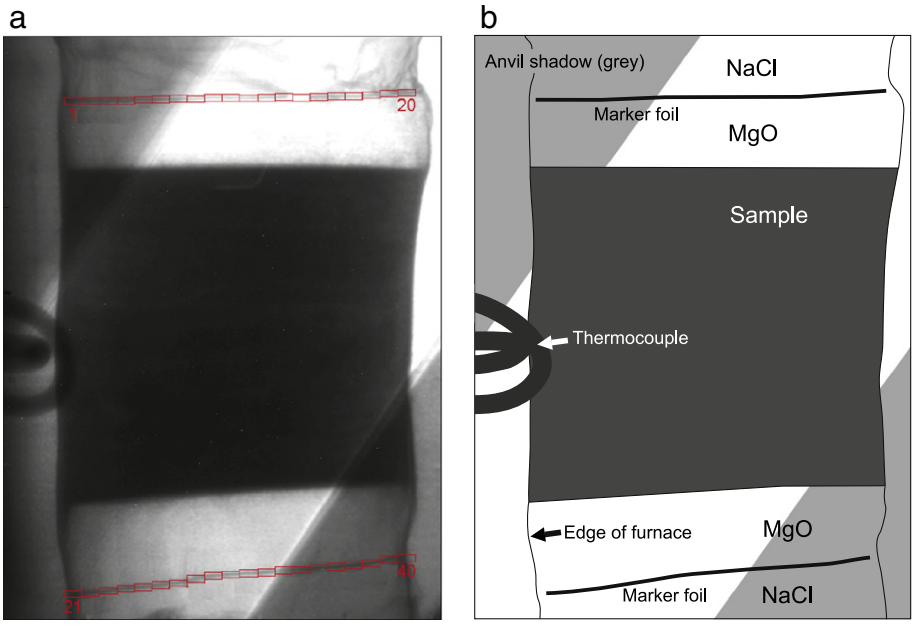

Fig. 2. (a) Example image from CaI_19, at 370 °C. This size of this image is 1360 by 1024 pixels (2720 × 2048 μm). The red boxes show the sub-sections of the image for which the displacements were calculated. (b) A simplified depiction highlighting the components observed in the radiography image.

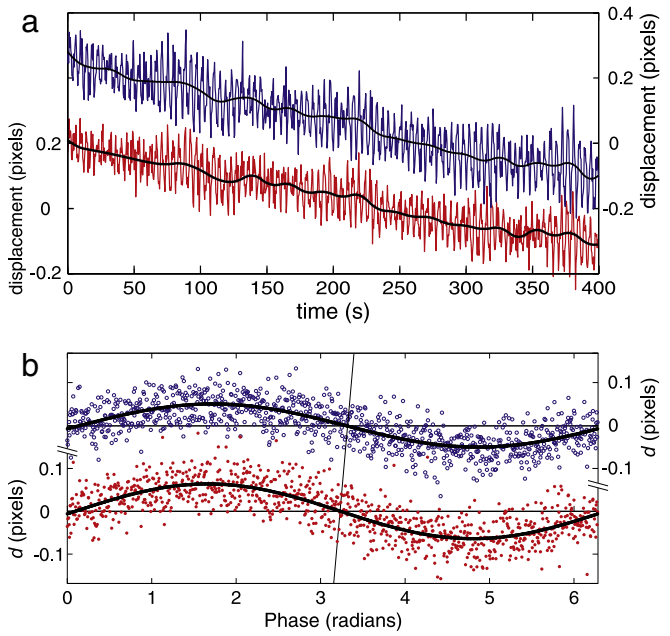

Fig. 3. (a) Raw displacement data at radii of 0.23 (top, blue) and 0.59 mm (bottom, red) from the 200 °C, 4 s data during CaI_19. The heavy black lines are the smoothing splines used to detrend the data. (b) The detrended data, as a function of phase angle, for the displacements shown in (a). The open circles correspond to the top displacement line and closed circles to the bottom; the thick lines are the fitted sine waves. The inclined line in the figure intersects both fitted curves at $d=0$ and illustrates the delay in the top curve relative to the bottom one (Φ in Eq. (1a)).

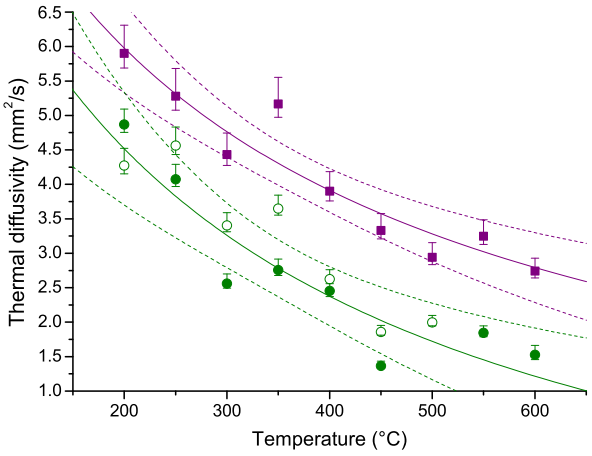

Fig. 4. Thermal diffusivity of perovskite (filled circles, green) and post-perovskite (filled squares, purple) structured $CaIrO_3$, from single foils. The open circles are the thermal diffusivities of perovskite–$CaIrO_3$ calculated from length change in sample. The two solid lines are the fit of $\kappa = a/T + b$ to the two single foil derived sets of values; the dashed lines are the 95% confidence intervals to the fits.

and discarded. The probability that a datum is outside of four standard deviations of the mean, for a normal distribution, is less than 7×10^{-5}. The fitted periods found across all temperatures and both experiments are very consistent, giving values of 8.124, 4.376, 2.500, 1.250 and 0.884 s, which correspond to the nominal periods of 8, 4, 2, 1 and 0.5 s respectively. For each nominal period the standard deviation of the calculated periods across all the data sets are of the order of 5×10^{-3} s and the standard errors of the well determined phases are of the order of 0.02 radians ($\approx 1.1°$).

The thermal diffusivity at each temperature was calculated from Eqs. (1a) and (1c) by minimising the weighted Sum Squared Differences; poorly determined and obviously erroneous phases were excluded from the fitting. The quality of the data precluded solving for R_0, which was therefore set to be approximately the centre-line of the furnace. The thermal diffusivity values for each phase are approximately linear in inverse absolute temperature; consistent with both simple theory (Hofmeister et al., 2007, and references therein) and the observations made in other studies (e.g. Osako and Ito, 1991). The semi-emperical relationship

$$\kappa = a/T + b \tag{3}$$

was therefore fitted to the data, from the single foil displacements, by minimising the sum squared differences, where T is the temperature in kelvins and a and b are coefficients. The quality of the data does not warrant using a more complex temperature dependency for the thermal diffusivity. As a test of the quality of these fits reduced chi squared values ($\tilde{\chi}$) were calculated for each fit, as were the 95% confidence intervals.

3. Results

The thermal diffusivities of perovskite and post-perovskite structured $CaIrO_3$ measured in this study are plotted in Fig. 4 and listed in Table 1. The solid lines in Fig. 4 are the fits of Eq. (3) to the single-foil thermal diffusivity values and the dashed lines are their corresponding 95% confidence intervals. There is a reasonable correspondence between the thermal diffusivities of the perovskite sample calculated from the length change (open circles, Fig. 4) and single foil (filled circles), validating the use of single foils as a way of calculating reliable thermal diffusivities. Eq. (3) provides a good description of the single-foil data with $\tilde{\chi}$ values of 0.16 and 0.23 for the perovskite and post-perovskite data respectively. At all temperatures investigated in this study the thermal diffusivity of post-perovskite is greater than that of perovskite. Above 200 °C the 95% confidence intervals do not overlap, therefore the difference between the measurements is robust and significant. The ratio of the difference between the measured values is reasonably constant above 275 °C (see Table 1); between 300 and 600 °C the thermal diffusivity of post-perovskite has a weighted average 1.8 ± 1 times greater than that of perovskite. The lower-temperature data, at 200 and 250 °C, are not included in this average because these values are not as accurate; this is due to

Table 1
Thermal diffusivity values for perovskite and post-perovskite structured $CaIrO_3$. These data have been plotted in Fig. 4. The numbers in brackets are the errors in the last figure of the value; for the ratios the errors are only asymmetrical in the 3rd significant figure and are therefore listed as single (symmetric) values. # denotes conditions at which data was collected but no reasonable thermal diffusivity could be calculated. The thermal diffusivity values from Cheng et al. (2011) and Keawprak et al. (2009) are included for comparison. *value for $CaSrO_3$.

Temperature	κ-perovskite		κ-post-perovskite	Ratio
	Single foil	Length change	Single foil	$\kappa_{p\text{-}pv}/\kappa_{pv}$
(°C)	(mm^2/s)	(mm^2/s)	(mm^2/s)	
This study				From single foils
200	$4.87(^{+22}_{-22})$	$4.28(^{+25}_{-12})$	$5.90(^{+41}_{-21})$	1.2(1)
250	$4.08(^{+21}_{-11})$	$4.57(^{+27}_{-12})$	$5.28(^{+40}_{-20})$	1.3(1)
300	$2.56(^{+14}_{-7})$	$3.40(^{+18}_{-9})$	$4.43(^{+31}_{-16})$	1.7(1)
350	$2.76(^{+16}_{-8})$	$3.65(^{+19}_{-10})$	$5.17(^{+39}_{-19})$	1.9(1)
400	$2.46(^{+17}_{-8})$	$2.63(^{+14}_{-7})$	$3.90(^{+28}_{-14})$	1.6(2)
450	$1.37(^{+7}_{-4})$	$1.86(^{+9}_{-4})$	$3.33(^{+25}_{-12})$	2.4(3)
500	#	$2.00(^{+10}_{-5})$	$2.94(^{+21}_{-11})$	
550	$1.85(^{+10}_{-6})$	#	$3.25(^{+24}_{-12})$	1.7(2)
600	$1.53(^{+14}_{-7})$	#	$2.74(^{+19}_{-10})$	1.8(3)
Cheng et al., 2011				
25	0.07(1)*		0.16(2)	2.4(6)*
Keawprak et al., 2009				
25	1.5		2.7	1.8

the amplitude of the thermal oscillations being large compared to the difference between the mean sample temperature (200 or 250 °C) and the room temperature sink.

The present results agree with previous studies in that post-perovskite is found to have a higher thermal diffusivity than perovskite by a factor of almost two (Cheng et al., 2011; Keawprak et al., 2009), however the absolute values of thermal diffusivity are some two to four times higher in the present study. This difference is likely due to differences in the methodologies employed by the different studies: The study of Keawprak et al. (2009) measured thermal diffusivity in samples containing around 35% porosity. This would substantially reduce the thermal conductivity by inhibiting heat transfer between poorly bonded grains. Whilst Cheng et al. (2011) used hot-pressed samples which should have been close to full density the solid-solutions which they studied should have had reduced lattice thermal diffusivity due to impurity scattering of phonons. Furthermore, both previous studies were performed with no confining pressure, meaning that the samples might have suffered from thermal fracturing, which would further reduce the measured thermal diffusivity. The present measurements did not suffer from porosity (being sintered and performed at high pressure) and were performed on a pure chemical system reducing the effect of impurity scattering.

Even though the confining pressure ensures there are no voids in our samples, there are other potential sources of error. The shadow of the furnace was sufficient to obscure one of the Pt foil strips in the images from experiment CaI_19 and it is therefore possible for it to have interfered with the measured thermal strain. The measured displacements are a convolution of the displacements of the foil strips and those of the furnace. The phase of this single displacement will be intermediate to that of the foil strips and the furnace; with the exact phase depending on the relative weighting of the two components. This means that the measured phase difference (Φ, Eq. (1a)) across the radius of the sample will be smaller than the true value. The thermal diffusivities associated with these phase differences will be larger than the actual values because larger thermal diffusivity values have smaller phase changes with increasing radius (Eq. (1a) and (1c)). It is not trivial to deconvolve the separate displacements (and therefore phases) of the furnace and the Pt foil strip because their shapes and relative weightings in the images are not known independently. Nevertheless, because the furnace and Pt strips are the same size and thickness in both experiments and the same size boxes are used to calculate the displacements, the furnace and Pt foil can be assumed to have the same weights in the displacement analysis and therefore have the same effect on the measurements.

Likewise, the MgO at the ends of the samples is another potential source of error. If the contribution to the measurement from the ~300 μm of MgO at the ends of sample is significant it will increase the absolute measured values because MgO has high heat transport properties (e.g. Hofmeister et al., 2007; Katsura, 1997). This will reduce the ratio of the measured thermal diffusivities and if the measurements were completely dominated by MgO there would be no distinguishable differences between the two phases. However, the amount of MgO in the experiments is small compared to the sample, there are similar amounts of MgO in both experiments and most importantly the ratio of the thermal diffusivities measured here is similar to those measured by Cheng et al. (2011) and Keawprak et al. (2009) at room temperature. Therefore, the measurements are not dominated by MgO but because we have not corrected for the contribution to the signal from MgO the measured ratio of the thermal diffusivities should be considered a minimum value.

The recovered samples were analysed by both X-ray diffraction and EBSD measurements. The post-perovskite sample (experiment CaI_19) is still pure phase but with a slight texture. The {010} planes of the post-perovskite are predominantly aligned parallel to the furnace axis; which is the commonly observed $CaIrO_3$–post-perovskite deformation texture (e.g. Walte et al., 2007; Yamazaki et al., 2006). The perovskite sample, on the other-hand, is predominantly perovskite with some post-perovskite in it and there is no significant texturing in the post-perovskite. The diffraction patterns acquired during the experiment are not of sufficient quality to determine at what temperature the sample started to transform from perovskite to post-perovskite. The presence of post-perovskite $CaIrO_3$ in the perovskite sample at high-temperatures reduces the difference between the measured thermal diffusivities.

The sources of error discussed above mean that the absolute values of thermal diffusivity measured in this study might not be accurate, they are however internally consistent. Given the significant differences between the methodologies of the three studies which have measured the thermal diffusivity of perovskite and post-perovskite, the excellent agreement in the relative thermal diffusivity of the two phases suggests that the observed difference in thermal diffusivity between perovskite and post-perovskite is robust.

4. Dynamical consequences: modelling

Preliminary investigations into the dynamical consequences of distinct diffusivity perovskite and post-perovskite were undertaken using the numerical model Fluidity (Davies et al., 2011). To isolate the effects of a contrasting thermal diffusivity, models were intentionally kept simple and only two cases were examined: a reference case where perovskite and post-perovskite had equal diffusivities and a second case where post-perovskite had a thermal diffusivity twice that of perovskite. All other model parameters were identical (note that key model parameters are listed in Table 2). Isoviscous extended Bousinessq convection was simulated at a Rayleigh number of 2×10^5 and a Dissipation number of 0.35, in a two-dimensional square domain of unit dimensions. To non-dimensionalize, spatial quantities were scaled with h, pressure with $\rho_0 g h$ and temperature with ΔT, where h, ρ_0, g and ΔT denote mantle depth, reference density, gravitational acceleration and the temperature difference across the domain, respectively. Free-slip and no penetration velocity boundary conditions were specified at all domain boundaries. Temperatures at the top and bottom of the domain were set to 0 and 1 respectively, whilst side-walls were insulating. A Clapeyron slope, the non-dimensional equivalent of $10\,\mathrm{MPaK}^{-1}$ (which is the middle of the range of published Clapeyron slopes for the $MgSiO_3$ phase transition; see Tateno et al., 2009; Catalli et al., 2009, and references therein), was specified for the perovskite to post-perovskite phase transition, whilst we ensured a double crossing of the post-perovskite stability field, as suggested by observations (e.g. Hernlund et al., 2005). Excluding the distinct thermal diffusivity, the post-perovskite field had no other distinctive material properties; no density contrast was included across the phase boundary, latent heat release was ignored and the rheology of perovskite and post-perovskite was identical. In effect, for the reference case, no post-perovskite was present but the region where it would form was tracked. We intentionally examined the system at a low Rayleigh number, allowing simulations to achieve a quasi steady-state solution that allows for straightforward comparison between different cases.

Table 2
Key model parameters.

Symbol	Meaning	Value
Ra_0	Reference Rayleigh Number	~2×105
Di	Dissipation number	~0.35
H	Mantle depth	2890 km
ρ_0	Reference density	3500 kg/m^3
g	Gravitational acceleration	9.81 m/s^2
ΔT	Temperature scale	3600 K
α	Thermal expansion coefficient	2.0×10^{-5} K^{-1}
μ	Viscosity	3.0×1023 Pa s
κ_0	Reference thermal diffusivity	1.0×10^{-6} m^2/s

The thermal field and post-perovskite regions of our simulations are illustrated in Fig. 5a and b for the contrasting diffusivity case and the reference case (equal diffusivity), respectively. As expected, post-perovskite occurs where the downwelling convective limb reaches the lowermost part of the domain. In both cases, the boundary between perovskite and post-perovskite is crossed twice by the local cold mantle geotherm (see Fig. 6) and, accordingly, post-perovskite occurs in 'lenses', which are separated from the CMB by a thin layer of perovskite. When compared to the reference case, doubling the thermal diffusivity of post-perovskite causes downwelling material to heat up comparatively quickly upon entry into the post-perovskite stability field (notice the temperature differences between the two simulations, plotted in Fig. 4). As a consequence, almost all parts of the mantle become hotter, the extent of the post-perovskite lens decreases, the upper and lower boundaries of the lens move deeper into the mantle and the upwelling becomes broader (compare extent of 0.5 isotherm in Fig. 5a and b, c). Perhaps surprisingly, doubling the thermal diffusivity also has the consequence of enhancing the convective heat transport, with the global RMS velocity increasing by around 2% when compared to the reference case; importantly, this increase in RMS velocity is not a consequence of rheological weakening as the models are isoviscous. Although variations in velocity occur throughout the domain (see Fig. 5d), this manifests itself predominantly as an increased velocity in the down-going convective limb with the convective planform becoming more asymmetric (when differences is the velocity fields between each case are plotted – Fig. 5d – velocity vectors shift towards the downwelling limb). Paradoxically, this increase in down-welling velocity occurs despite a minor increase in the temperature of the down-welling limb (Fig. 6a). Although, the increased diffusivity post-perovskite does not come into contact with the CMB, surface and CMB heat fluxes increase by around 4%, when compared to the reference case. The lowermost mantle geotherms illustrated in Fig. 6b demonstrate why: the vertical temperature gradient decreases in the higher diffusivity post-perovskite lenses, due to more efficient conductive heat transport. However, owing to the isothermal boundary condition at the CMB, vertical temperature gradients within the perovskite, below the post-perovskite lenses, must increase and, accordingly, so does the CMB heat flux. The increased diffusivity post-perovskite lenses therefore act to draw heat vertically into the mantle. Moreover, lateral variations in CMB heat-flux increase as thermal gradients are higher below post-perovskite lenses and lower under upwellings (Fig. 6b).

5. Discussion

The experiments undertaken in this study confirm that post-perovskite–$CaIrO_3$ has at least 1.8 ± 1 times the thermal diffusivity of perovskite–$CaIrO_3$ at elevated temperatures (Fig. 4, Table 1). This ratio of thermal diffusivities is consistent with the ambient temperature measurements of Cheng et al. (2011) and Keawprak et al. (2009) and the predictions of Hofmeister (2007). This result lead us to undertake simplified modelling of the dynamical consequences of a post-perovskite layer with greater thermal transport properties than the surrounding perovskite. Even though the post-perovskite does not contact the CMB, conductive post-perovskite leads to an increase in the CMB heat flux when compared to the reference case; this, in turn, increases the surface heat flux and mean mantle temperature. The RMS flow velocity also shows an increase over the reference case, despite the isoviscous rheology. Lateral variations in heat flux increase and the convective planform becomes more Earth-like, with the down-going convective limb becoming stronger than the up-welling limb. Up-

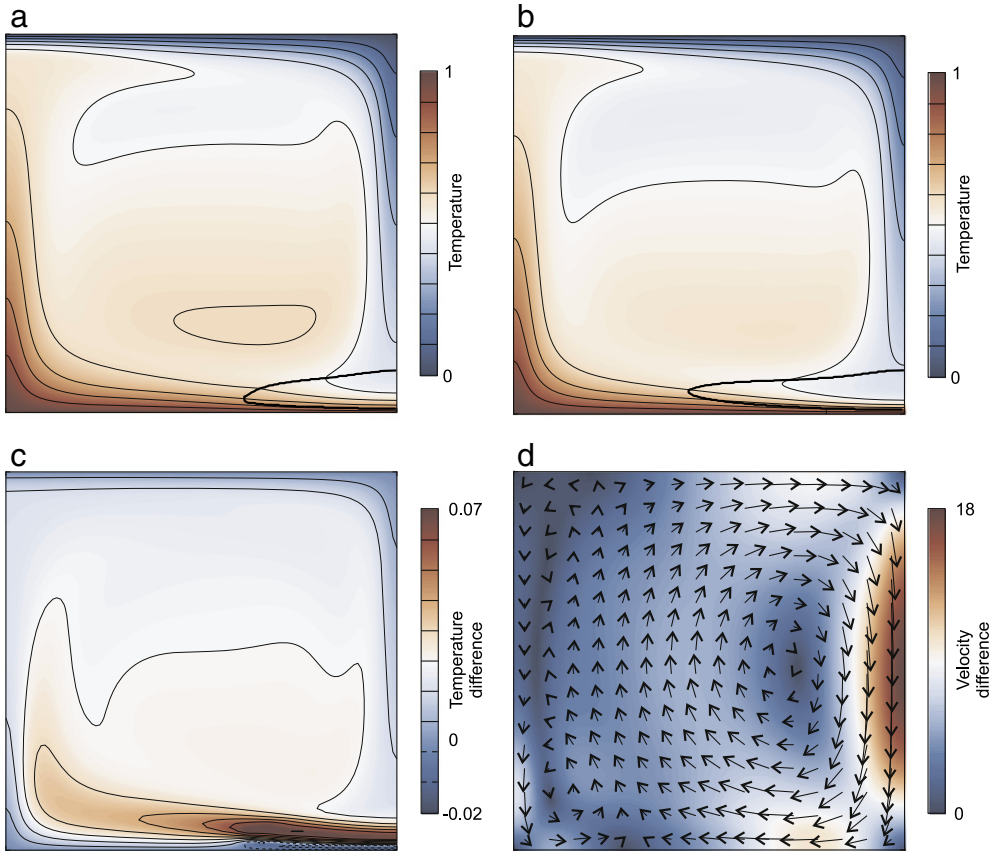

Fig. 5. Non-dimensional temperature fields from simulations with (a) contrasting and (b) equal diffusivity post-perovskite. The thick black line is the perovskite–post-perovskite phase boundary. The differences (contrasting diffusivity − equal diffusivity) in (c) temperature and (d) velocity magnitude between both cases (contrasting κ ppv − equal κ ppv) are also included. The arrows in figure (d) are the difference in the velocity vectors between the two simulations. The contours are at intervals of 0.1 dimensionless temperature in (a) and (b) and at intervals of 0.009 in (c); in (d) the length of the arrow stem is proportional to the velocity.

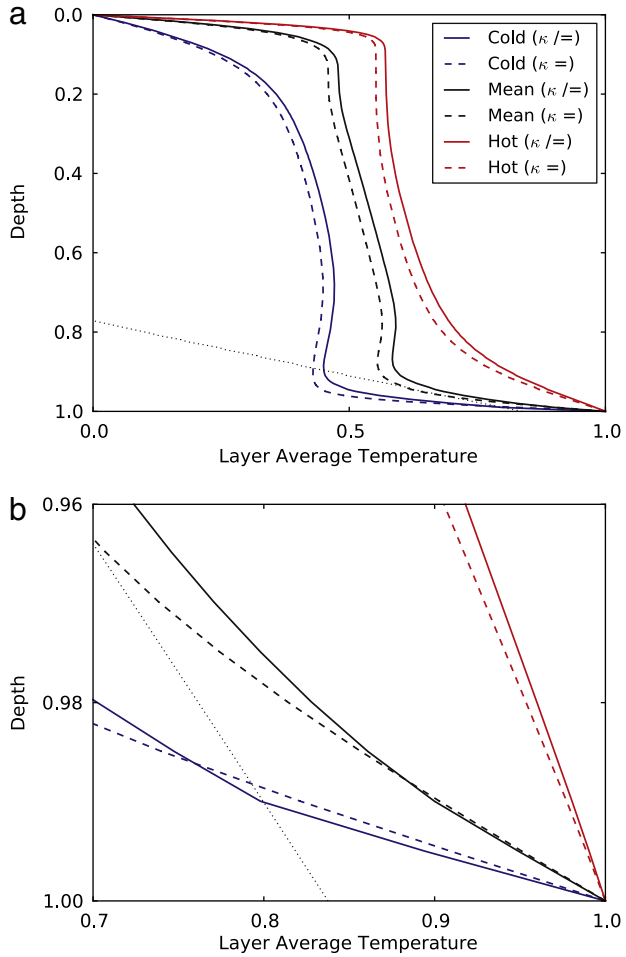

Fig. 6. (a) Average temperatures for upwelling (hot/red) and downwelling (cold/blue) sections of the convecting system, for simulations with equal ($\kappa=$; dashed lines) and contrasting ($\kappa/=$; continuous lines) perovskite/post-perovskite diffusivities. Mean layer temperatures from both cases are also included for comparison (black); (b) as in a, but focussed upon the lowermost region of the domain. The perovskite–post-perovskite phase boundary is marked by the black dotted line. Note the sharp change in temperature gradient as material enters contrasting diffusivity post-perovskite (continuous blue line).

wellings also become broader, consistent with the study of Matyska and Yuen (2006). The effects of increased thermal diffusivity in post-perovskite are similar to those observed by Nakagawa and Tackley (2004), who examined the dynamical consequences of a density change and latent heat release across the phase transition. It is therefore likely that these effects will combine, thus having an important influence on mantle dynamics. This implies that the distinct properties of a post-perovskite phase should not be neglected in simulations of mantle convection.

Whilst the mean thermal diffusivity of post-perovskite, measured here, is approximately twice that of perovskite this value is likely only applicable to samples with uniformally distributed poly-crystalline post-perovskite. Post-perovskite is structurally anisotropic and olivine, which is much less anisotropic than post-perovskite, has been observed to have 73% anisotropy in thermal transport properties between the a and b crystallographic directions (Chai et al., 1996). It is likely, therefore, that the thermal transport properties of single-crystal post-perovskite will be extremely anisotropic. This, combined with a high degree of lattice preferred orientation in the post-perovskite, is expected therefore to have a significant impact on the direction and magnitude of heat flow in the lowermost mantle.

Furthermore, whilst the results of our dynamical modelling doubtlessly provide interesting insights, they have been examined at a relatively low Rayleigh number and, therefore, are not directly applicable to Earth's mantle. They should only be considered qualitatively: it is important to examine such cases in 3-D spherical geometry, at a Rayleigh number applicable to Earth's mantle (e.g. Davies and Davies, 2009; Nakagawa and Tackley, 2011; Wolstencroft et al., 2009). It is also important to consider the combined effects of variations in rheological and other thermal transport properties of post-perovskite, which has not been done here (Nakagawa and Tackley, 2011; Tosi et al., 2010).

Despite these caveats, the simple convection models presented imply that heat transport across Earth's core–mantle-boundary is greater than previously assumed, and may exceed the 13(4) TW suggested by Lay et al. (2006). It is therefore a substantial contributor to Earth's present day surface heat flux of 47(2) TW (as per Davies and Davies, 2010). Furthermore, over geological time, secular cooling of Earth's mantle will be buffered by the development of post-perovskite in D″. This buffering will occur at the expense of Earth's core, which will cool faster than in the absence of post-perovskite. In turn, this implies that the inner-core might be younger than previously regarded (e.g. Butler et al., 2005; Labrosse et al., 2001).

Acknowledgements

SAH (NE/H016309/1), DRD (NE/H015329/1) and AMW (NE/E012922/2) were funded by NERC post-doctoral research fellowships; SAH and LL were funded by NSF grant EAR0809397. RJMcC was funded the by the European Commission through the Marie Curie Research Training Network "c2c" contract no. MRTN-CT-2006-035957. Use of the National Synchrotron Light Source, Brookhaven National Laboratory, was supported by the U.S. Department of Energy, Office of Science, Office of Basic Energy Sciences, under contract no. DE-AC02-98CH10886. Use of the X17B2 beamline was supported by COMPRES, the Consortium for Materials Properties Research in Earth Sciences under NSF Cooperative Agreement EAR 10-43050 and by the Mineral Physics Institute, Stony Brook University. DRD would like to acknowledge the Applied Modelling and Computation Group (AMCG) at Imperial College London, particularly Stephen Kramer and Cian Wilson, for support and advice with development of Fluidity. We thank two anonymous reviewers for their helpful comments and suggestions.

References

Ammann, M.W., Brodholt, J.P., Dobson, D.P., 2010. First-principles constraints on diffusion in lower-mantle minerals and a weak D″ layer. Nature 465, 462–465.
Butler, S., Peltier, W., Costin, S., 2005. Numerical models of the Earth's thermal history: effects of inner-core solidification and core potassium. Phys. Earth Planet. Inter. 152 (1–2), 22–42.
Catalli, K., Shim, S.-H., Prakapenka, V., 2009. Thickness and clapeyron slope of the post-perovskite boundary. Nature 462 (7274), 782–785 Dec..
Chai, M., Brown, J.M., Slutsky, L.J., 1996. Thermal diffusivity of mantle minerals. Phys. Chem. Miner. 23, 470–475.
Cheng, J.-G., Zhou, J.-S., Goodenough, J.B., Sui, Y., Ren, Y., Suchomel, M.R., 2011. High-pressure synthesis and physical properties of perovskite and post-perovskite $Ca_{1-x}Sr_xIrO_3$. Phys. Rev. B 83 (6), 064401 Feb..
Davies, D.R., Davies, J.H., 2009. Thermally-driven mantle plumes reconcile multiple hot-spot observations. Earth Planet. Sci. Lett. 278, 50–54. doi:10.1016/j.epsl.2008.11.027.
Davies, J.H., Davies, D.R., 2010. Earth's surface heat flux. Solid Earth 1, 5–24. doi:10.5194/se-1-5-2010.
Davies, D.R., Wilson, C.R., Kramer, S.C., 2011. Fluidity: a fully unstructured anisotropic adaptive mesh computational modeling framework for geodynamics. Geochem. Geophys. Geosys. 12, Q06001. doi:10.1029/2011GC003551.
Dobson, D.P., Hunt, S.A., Li, L., Weidner, D.J., 2008. Measurement of thermal diffusivity at high pressures and temperatures using synchrotron radiography. Mineral. Mag. 72 (2), 653–658. doi:10.1180/minmag.2008.072.2.653.
Dobson, D.P., Hunt, S.A., McCormack, R., Lord, O.T., Weidner, D.J., Li, L., Walker, A.M., 2010. Thermal diffusivity of MORB-composition rocks to 15 GPa: implications for triggering of deep seismicity. High Pressure Res. 30 (3), 406–414. doi:10.1080/08957959.2010.516827.
Garnero, E.J., Lay, T., 2003. D″ shear velocity heterogeneity, anisotropy and discontinuity structure beneath the Caribbean and Central America. Phys. Earth Planet. Inter. 140 (1-3), 219–242 geophysical and Geochemical Evolution of the Deep Earth.

Guignot, N., Andrault, D., Morard, G., Bolfan-Casanova, N., Mezouar, M., 2007. Thermoelastic properties of post-perovskite phase $MgSiO_3$ determined experimentally at core-mantle boundary P–T conditions. Earth Planet. Sci. Lett. 256 (1–2), 162–168.
Hernlund, J.W., Thomas, C., Tackley, P.J., 2005. A doubling of the post-perovskite phase boundary and structure of the Earth's lowermost mantle. Nature 434, 882–886.
Hofmeister, A.M., 2007. Thermal conductivity of Earth's deepest Mantle. In: Yuen, D., Maruyama, S., Karato, S., Windley, B. (Eds.), Superplumes: Beyond Plate Tectonics. Springerlink, pp. 269–292. Ch. 10.
Hofmeister, A.M., 2010. Thermal diffusivity of oxide perovskite compounds at elevated temperature. J. Appl. Phys. 107, 103532.
Hofmeister, A.M., Branlund, J.M., Pertermann, M., 2007. Properties of rock and minerals — thermal conductivity of the earth. In: Schubert, G. (Ed.), Treatise in Geophysics. : Vol. 2 of Treatise in Geophysics. Elsevier, pp. 543–577.
Hunt, S.A., Weidner, D.J., Li, L., Wang, L., Walte, N., Brodholt, J.P., Dobson, D.P., 2009. Weakening of $CaIrO_3$ during the perovskite-post perovskite transformation. Nat. Geosci. 2, 794–797. doi:10.1038/NGEO663.
Hunt, S.A., Walker, A.M., McCormack, R., Dobson, D.P., Wills, A.S., Li, L., 2011. The effect of pressure on thermal diffusivity in pyroxenes. Mineral. Mag. 75 (5), 2597–2610. doi:10.1180/minmag.2011.075.5.2597.
Katsura, T., 1993. Thermal diffusivity of silica glass at pressures up to 9 GPa. Phys. Chem. Miner. 20, 201–208.
Katsura, T., 1995. Thermal diffusivity of olivine under upper mantle conditions. Geophys. J. Int. 122, 63–69.
Katsura, T., 1997. Thermal diffusivity of periclase at high temperatures and high pressures. Phys. Earth Planet. Inter. 101, 73–77.
Keawprak, N., Tu, R., Goto, T., 2009. Thermoelectrisity of $CaIrO_3$ ceramics prepared by spark plasma sintering. J. Ceram. Soc. Jpn. 117 (4), 466–469.
Khedari, J., Benigni, P., Rogez, J., Mathieu, J., 1995. New apparatus for thermal-diffusivity measurements of refractory solid materials by the periodic stationary method. Rev. Sci. Instrum. 66, 193–198.
Komabayashi, T., Hirose, K., Sugimura, E., Sata, N., Ohishi, Y., Dubrovinsky, L.S., 2008. Simultaneous volume measurements of post-perovskite and perovskite in $MgSiO_3$ and their thermal equations of state. Earth Planet. Sci. Lett. 265 (3–4), 515–524.
Labrosse, S., Poirier, J.-P., Moul, J.-L.L., 2001. The age of the inner core. Earth Planet. Sci. Lett. 190 (3–4), 111–123.
Lay, T., Hernulnd, J., Garnero, E.J., Thorne, M.S., 2006. A post-perovskite lens and D″ heat flux beneath the central pacific. Science 314, 1272–1276.
Lindsay-Scott, A., Wood, I.G., Dobson, D.P., 2007. Thermal expansion of $CaIrO_3$ determined by X-ray powder diffraction. Phys. Earth Planet. Inter. 162, 140–148.
Manthilake, G.M., de Koker, N., Frost, D.J., McCammon, C.A., 2011. Lattice thermal conductivity of lower mantle minerals and heat flux from earth's core. Proc. Natl. Acad. Sci. 108 (44), 17901–17904.
Martin, D.C., Chapman, K.W., Chupas, P.J., Parakapenka, V., Lee, P.L., Shastri, S.D., Parise, J.B., 2007. Compression, thermal expansion, structure, and instability of $CaIrO_3$, the structure model of $MgSiO_3$ post-perovskite. Am. Mineral. 92, 1048–1053.
Matyska, C., Yuen, D.A., 2006. Lower mantle dynamics with the post-perovskite phase change, radiative thermal conductivity, temperature- and depth-dependent viscosity. Phys. Earth Planet. Inter. 154 (2), 196–207.
Murakami, M., Hirose, K., Kawamura, K., Sata, N., Ohishi, Y., 2004. Post-perovskite phase transition in $MgSiO_3$. Science 304, 855–858.
Nakagawa, T., Tackley, P.J., 2004. Effects of a perovskite-post perovskite phase change near the core-mantle boundary in compressible mantle convection. Geophys. Res. Lett. 32.
Nakagawa, T., Tackley, P.J., 2011. Effects of low-viscosity post-perovskite on thermo-chemical mantle convection in a 3-D spherical shell. Geophys. Res. Lett. 38.
Oganov, A.R., Ono, S., 2004. Theoretical and experimental evidence for a post-perovskite phase of $MgSiO_3$ in the Earth's D″′ layer. Nature 430, 445–448.
Osako, M., Ito, E., 1991. Thermal diffusivity of $MgSiO_3$ perovskite. Geophys. Res. Lett. 18 (2), 239–242.
Panning, M., Romanowicz, B., 2004. Inferences on flow at the base of Earth's mantle based on seismic anisotropy. Science 303 (5656), 351–353.
Schubert, G., Turcotte, D.L., Olson, P., 2001. Mantle Convection in the Earth and Planets. Cambridge University Press, Cambridge.
Tateno, S., Hirose, K., Sata, N., Ohishi, Y., 2009. Determination of post-perovskite phase transition boundary up to 4400 K and implications for thermal structure in D″ layer. Earth Planet. Sci. Lett. 277 (1–2), 130–136.
Tosi, N., Čadek, O., Martinec, Z., Yuen, D.A., Kaufmann, G., 2009. Is the long-wavelength geoid sensitive to the presence of postperovskite above the core-mantle boundary? Geophys. Res. Lett. 36 (5), L05303 Mar..
Tosi, N., Yuen, D.A., Cadek, O., 2010. Dynamical consequences in the lower mantle with the post-perovskite phase change and strongly depth-dependent thermodynamic and transport properties. Earth Planet. Sci. Lett. 298, 229–243.
Vaughan, M., Weidner, D.J., Wang, Y., Chen, J.H., Koleda, C.C., Getting, I.C., 1998. T-cup: a new high-pressure apparatus for X-ray studies. Rev. High Pressure Sci. Technol. 7, 1520–1522.
Walker, A., Forte, A.M., Wookey, J., Nowacki, A., Kendall, J.-M.M., 2011. Elastic anisotropy of D″′ predicted from global models of mantle flow. Geochem. Geophys. Geosyst. 12, Q10006.
Walte, N., Heidelbach, F., Miyajima, N., Frost, D.J., 2007. Texture development and TEM analysis of deformed $CaIrO_3$: implications for the D″ layer at the core-mantle boundary. Geophys. Res. Lett. 34, L08306.
Wolstencroft, M., Davies, J.H., Davies, D.R., 2009. Nusselt–Rayleigh number scaling for spherical shell Earth mantle simulations up to a Rayleigh number of 10^9. Phys. Earth Planet. Inter. 176, 132–141. doi:10.1016/j.pepi.2009.05.002.
Xu, Y., Shankland, T.J., Linhardt, S., Rubie, D.C., Langenhorst, F., Klasinski, K., 2004. Thermal diffusivity and conductivity of olivine, wadsleyite and ringwoodite to 20 GPa and 1373 K. Phys. Earth Planet. Inter. 143–144, 321–336.
Yamazaki, D., Yoshino, T., Ohfuji, H., Ando, J.-i., Yoneda, A., 2006. Origin of seismic anisotropy in the D″ layer inferred from shear deformation experiments on post-perovskite phase. Earth Planet. Sci. Lett. 252, 372–378.